Facilitating the Identification of the Soft Zone in a 1.25Cr-0.5Mo Heat-Resistant Steel

YANG SHEN, ZHENGMAN GU, and CONG WANG

A novel technique, by implementing a well-designed simulated welding, is proposed to precisely locate the soft zone. We capture and demonstrate that essential factors, including hardness profiles, geometrical dimension, microstructures, and elemental distributions, could enable fair comparison of key heat-affected zone sub-regions between actual and simulated welding samples. It is found that the width of the heat-affected zone has been expanded approximately 3 times, which will unambiguously facilitate the identification of the elusive soft zone.

https://doi.org/10.1007/s11663-021-02193-8

1.25Cr-0.5Mo steel is one of the most versatile Cr-Mo series of heat-resistant steels and has been extensively employed for boilers, coke drums, and heat exchangers.[1–3] Low heat input welding techniques are commonly used to weld such heat-resistant steel grade for manufacturing large pressure vessel components.[4–6] However, one of the serious problems is the reduced creep rupture strength of the heat-affected zone (HAZ), resulting premature failure of the weldments during long-term service.[7,8] Moreover, HAZ is generally a confined space (only 2–3 mm in width), but categorized into three or even more narrow sub-zones, including coarse-grained heat-affected zone (CGHAZ), fine-grained heat-affected zone (FGHAZ), and intercritical heat-affected zone (ICHAZ),[9–11] which pose significant challenges in pinpointing the exact location leading to creep rupture and assessing residual lifetime.[12,13]

Tremendous investigations have been conducted to trace the initiation of creep cavities and associated creep rupture mechanisms.[14–17] One common consensus is that the region where the infamously premature and insidious creep failure occurs during high-temperature service invariably shows the lowest hardness values,[18] which is identified as the soft zone. However, the precise location of the soft zone has been inconsistently reported as occurring in either the FGHAZ, the ICHAZ, or even the over-tempered base metal (BM) in different studies.[19,20] Abd El-Azim *et al.*[21] have found that the soft zone of P91 welded joints was located in the FGHAZ, which controlled the creep rupture strength and minimum creep rate of the welded joints. Laha *et al.*[22] have shown that the soft zone of the modified 9Cr-1Mo welded joints occurred in the ICHAZ, and preferential accumulation of creep deformation coupled with extensive creep cavitation in the ICHAZ led to type IV cracking. Pandey *et al.*[23] have investigated the effect of post-weld heat treatment conditions on creep fracture behaviors of P91 welded joints and revealed that a shift in fracture location was observed from FGHAZ/ICHAZ to over-tempered BM after normalizing and tempering.

To overcome this hurdle of paramount significance, numerous efforts have been exercised to physically simulate HAZs to achieve comparable technical analogies. One approach is to isothermally heat the whole of the specimens to the desired peak temperatures to reproduce microstructure of corresponding region. Fujibayashi *et al.*,[24] by employing heat treatments, successfully simulated the microstructure of the ICHAZ of a 1.25Cr-0.5Mo heat-resistant steel to explore the effect of carbide morphology on the susceptibility to type IV cracking. However, it needs to be pointed out that actual welding is a rather complicated process due to drastic heating and cooling rates, which may not be accurately achieved by heat treatment process. Albert *et al.*,[25] when performing creep tests using specimens with CGHAZ microstructures simulated at the center, maneuvered a scheme where the creep fracture similar to type IV fracture in ferritic steel welded joints by employing a weld simulator (Gleeble 1500) to enable a well-controlled CGHAZ. Furthermore, Bhaduri *et al.*[26] demonstrated the deformation behavior of Gleeble-simulated ICHAZ on a modified 9Cr-1Mo steel and indicated that the ICHAZ with the larger prior austenite grain (PAG) size is more resistant to deformation than the smaller PAG size.

YANG SHEN and ZHENGMAN GU are with the School of Metallurgy, Northeastern University, Shenyang 110819, P.R. China. CONG WANG is with the School of Metallurgy, Northeastern University and also with the State Key Laboratory of Rolling and Automation, Northeastern University, Shenyang 110819, P.R. China. Contact e-mail: wangc@smm.neu.edu.cn

Manuscript submitted February 21, 2021, accepted April 16, 2021.

Published online: 10 May 2021

The identification and location of soft zone is crucial for heat-resistant steel development, which could potentially facilitate the understanding of creep fracture mechanisms during long-term creep tests. Nevertheless, until now, in-depth investigations on microstructural features and formation mechanism of the soft zone remain scare as most of the available techniques are not able to scale up and pinpoint the soft zone. Therefore, in the present work, a novel method by using a Gleeble weld simulator is proposed to amplify the highly narrow HAZ of a 1.25Cr-0.5Mo steel and precisely identify the region of the soft zone by capturing and demonstrating the essential factors between actually welded and simulated samples.

The chemical composition of the as-received 1.25Cr-0.5Mo steel (ASTM A378 Grade 11 Class 2) is shown in Table I.

After initial thermomechanical processing, the steel plates were normalized at 1203 K for 52 minutes and tempered at 1033 K for 91 minutes, as shown in Figure 1(a). These base materials were used for designated actual welding and simulated welding. For convenience, the actual welding samples and the simulated welding samples are designed as 'AW' and 'SW' throughout the text, respectively.

For AW, two 26 mm thick steel plates with a 60 deg double-V weld groove and 2 mm root face were welded together by multilayer shielded metal arc welding (SMAW), as shown in Figure 1(c). SMAW parameters applied for the filling passes were 22 V, 115 A DC, 1.0–1.7 mm/s welding speed, and 11–19 kJ/cm heat input, respectively. For SW, the steel plate was machined into cuboid samples with dimensions of $11 \times 11 \times 80$ mm on a thermal-mechanical simulator (Gleeble 3500, Dynamic system INC., USA). As shown in Figure 1(b), thermal cycle was described by employing the Rykalin-3D heat transfer model, and corresponding experimental parameters were input in the control computer, such as pre-heating temperature (473 K), material density (7.85 g/cm^3), specific heat (0.46 J/(g K)), and thermal conductivity (0.45 J/(cm s K)). The peak welding temperature was set at 1673 K with a holding time of 1 second, and the targeted heat input was estimated to be 12 kJ/cm corresponding to the cooling times from 1073 K to 773 K ($t_{8/5}$) of 7.07 seconds, which guaranteed heat input consistency between AW and SW. After welding, AW and SW samples were further treated *via* post-weld heat treatment (PWHT) at 963 K for 6 hours, which were labeled as 'A6' and 'S6', respectively, hereinafter. A detailed description of the designed PWHT procedures is given elsewhere.[27]

The positions of the test specimens, which are marked by green rectangles, are illustrated in Figure 1(d). For microstructure and mechanical properties characterization, cross-sectional specimens were cut from the as-welded and PWHT samples. These specimens were prepared by standard metallographic procedures, which consist of mechanical grinding, polishing, and chemical etching with 4 pct nital. The macrographs of the AW and SW weldments were examined by a stereo microscope (SZ61TR, Olympus, Japan). Microstructural features were characterized by a field-emission scanning electron microscope (FESEM, MAIA3 XMH, TESCAN, CZ) operating at 20.0 kV acceleration voltage. Elemental distribution was revealed by an electro-probe microanalyzer (EPMA, JXA-8530F, JEOL, Japan) combined with a wavelength-dispersive X-ray spectroscope (WDS). More detailed descriptions of EPMA specimen preparation are presented elsewhere.[28] In addition, micro Vickers hardness across the cross-sections of etched specimens was measured with a load of 0.2 kgf, a dwell time of 12 seconds, and an indentation spacing of 200 μm with the straight lines themselves separated by a distance of 1 mm by using a microhardness tester (HXD-1000TMC/LCD, China). Three lines were obtained to ensure repeatability.

A typical microstructure of the as-received 1.25Cr-0.5Mo steel BM is presented in Figure 2. The microstructure is characterized by major components including polygonal ferrite and pearlite,[29] whose volume fractions are 61.9 $\pm$ 3.6 and 38.1 $\pm$ 3.6 pct, respectively (ASTM E 562 (also ISO 9042)). The average grain size of ferrite is 11.7 μm, which was measured from SEM images by the intercept method (ASTM E12) using the ImageJ software.[30] Figures 2(b) and (c) display typical secondary electron (SE) and back-scattered electron (BSE) images of BM. Figures 2(d) through (f) illustrate that distributions of Cr, Mo, and Fe are uniform in the BM. However, C distribution, as shown in Figure 2(g), exhibits large variations, which correspond to the presence of pearlite, and is consistent with SEM observation.

Figures 3(a) and (e) show micro Vickers hardness distribution characteristics across the width at defined intervals of the HAZs of AW and SW in the as-welded state. Corresponding macrostructures with micro Vickers hardness indentation are also offered in the insets of Figures 3(a) and (e). Corresponding CGHAZ, FGHAZ, and ICHAZ are clearly defined by commensurate micro Vickers hardness magnitudes.

As the peak temperature gradually decreases from the CGHAZ, to the FGHAZ, and to the ICHAZ, the micro Vickers hardness value diminishes concurrently. As shown in Figure 3(a), The CGHAZ-AW exhibits the highest micro Vickers hardness of 315.8 HV0.2 because of the bainitic structure within the coarse prior austenite grains (PAGs) formed upon active cooling.[31] The FGHAZ-AW features a lower micro Vickers hardness of 226.7 HV0.2 due to the undissolved and coarse carbides.[9,32] As ferrites and pearlites in the ICHAZ could be over-tempered,[33] the micro Vickers hardness value drops to 205.6 HV0.2, which is comparable to that of the BM (203.3 HV0.2). Moreover, as shown in Figure 3(e), it is demonstrated that the micro Vickers hardness values for each sub-zones of the SW sample show the same trend, decreasing from 317.9 HV0.2 (CGHAZ-SW) to 296.8 HV0.2 (FGHAZ-SW), and eventually to 208.6 HV0.2 (ICHAZ-SW). The slightly lowered micro Vickers hardness values in the sub-zones of the AW sample is largely caused by the tempering effects incurred by subsequent filling passes.[34,35]

Another interesting aspect to examine is on the dimension of the sub-zones of AW and SW, which is

Table I. Chemical Composition of 1.25Cr-0.5Mo Steel (Weight Percent)

C	Si	Mn	Cu	Ni	Cr	Mo	P	S
0.13	0.59	0.54	0.04	0.02	1.12	0.572	0.017	0.003

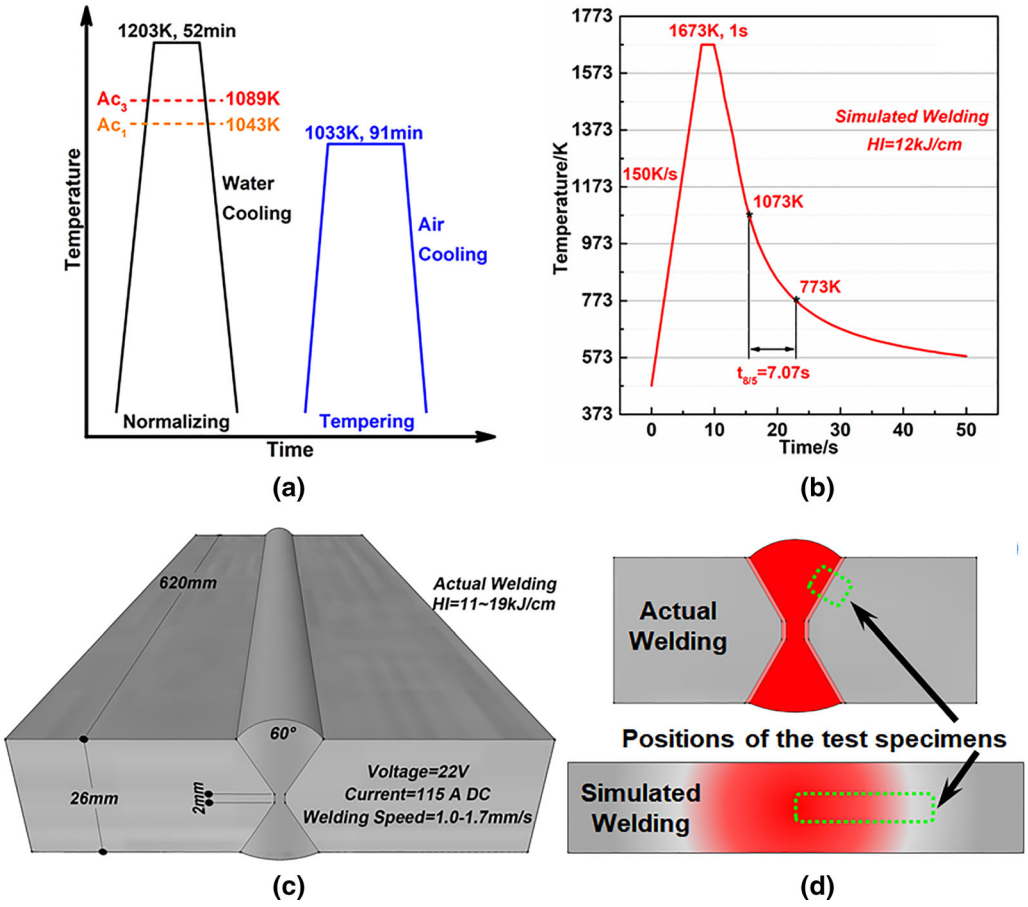

Fig. 1—Thermal cycles of (*a*) normalizing and tempering heat treatment and (*b*) simulated welding; schematic diagrams of (*c*) actual welding weldment and (*d*) cross-section of actual welding and simulated welding weldments showing the positions where specimens for desired tests are taken. (The regions marked by green rectangles are used for microstructure observations and micro Vickers hardness measurements) (Color figure online).

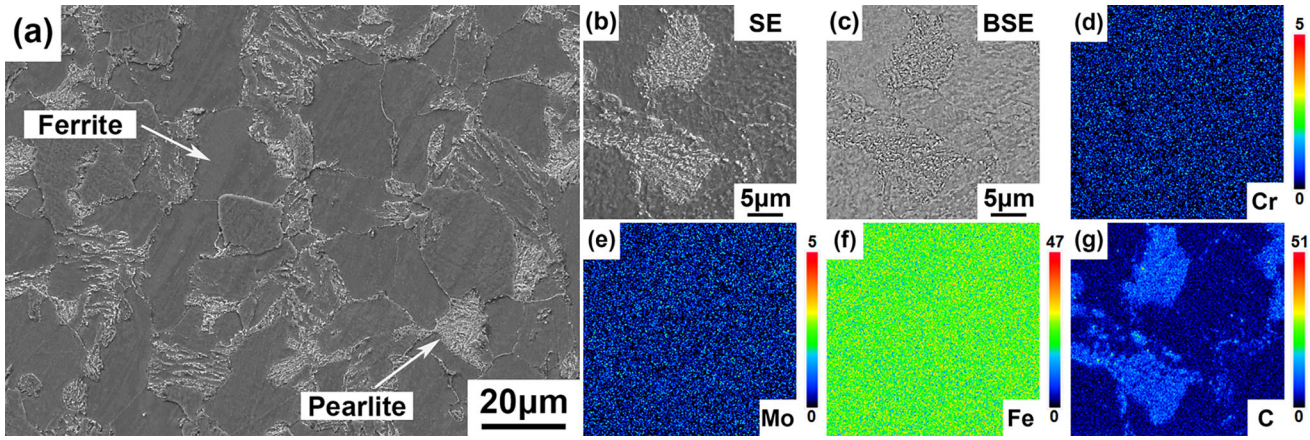

Fig. 2—Typical microstructural features of the 1.25Cr-0.5Mo steel base metal: (*a*) SEM micrograph; (*b*) through (*g*) EPMA results showing the distributions of Cr, Mo, Fe, and C.

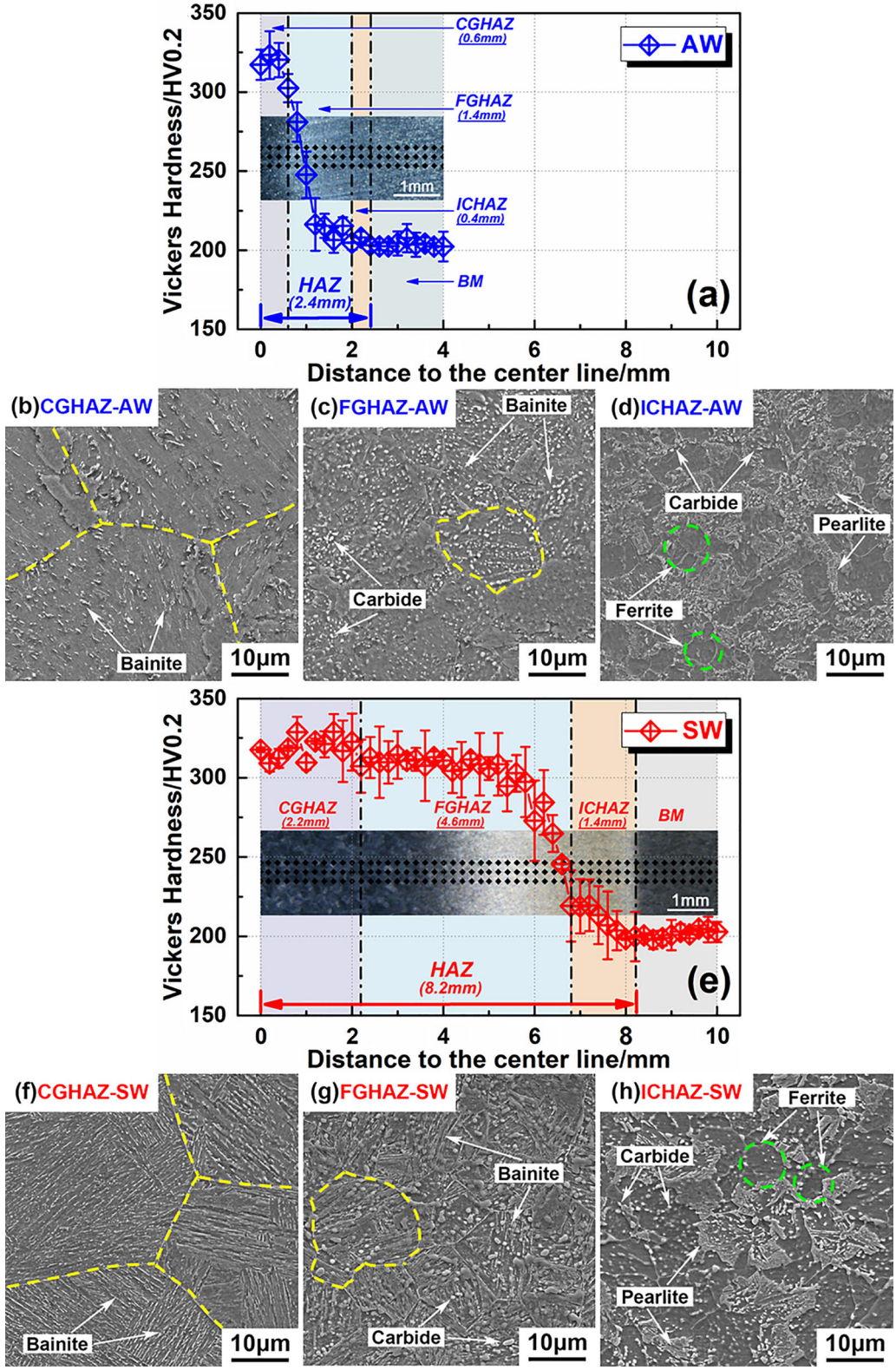

Fig. 3—Micro Vickers hardness profiles across the entire HAZ with the macrostructures of (*a*) AW and (*e*) SW weldments (Three different sub-zones of the HAZ are represented by different colors); SEM micrographs showing the microstructure of the sub-zones of the HAZ in AW (*b*, *c*, *d*) and SW (*f*, *g*, *h*): (b) and (f) CGHAZ, (c) and (g) FGHAZ, and (d) and (h) ICHAZ. (Yellow and green dash lines represent boundaries of prior austenite grain boundaries and equiaxed ferrites, respectively) (Color figure online).

illustrated by the width of the HAZ quantified in Figures 3(a) and (e). It is observed that the total widths of the HAZ in AW and SW are 2.4 and 8.2 mm, respectively. Furthermore, the widths of the CGHAZ, FGHAZ, and ICHAZ in the AW are 0.6, 1.4, and 0.4 mm, respectively. However, the widths of corresponding sub-zones in the SW are expanded to 2.2, 4.6, and 1.4 mm, respectively. A surprising finding is that both the total width of the HAZ in the SW and divided width of each sub-zone are approximately 3 times wider than those of AW. Such sizable expansion, coupled with comparable micro Vickers hardness values, could facilitate precise positioning of the soft zone.

Figures 3(b) through (d) and (f) through (h) show representative heterogeneous microstructures in the HAZ of AW and SW, respectively. Due to the high peak temperature (significantly higher than Ac_3, 1089 K) and long soaking time, ferrites and pearlites in the BM may likely transform into coarse austenite grains in the CGHAZ during the heating cycles.[36,37] Figure 3(b) shows the bainitic laths and bainitic granules within the coarse PAGs with an average size of 122 μm in the CGHAZ-AW. The microstructure of the CGHAZ-SW is also characterized by bainites with coarse PAGs (110 μm), as shown in Figure 3(f). Figure 3(c) presents the fine equiaxed PAGs structure in the FGHAZ-AW. The substructures mainly consist of bainite and carbides within fine PAGs (average size of 38.6 μm). Similarly, the microstructure of FGHAZ-SW is also composed of bainite and carbides, and PAGs, indicated by yellow dash lines in Figure 3(g), have an average grain size of 29.8 μm. The growth of austenitic grains is limited because of the pinning force from the undissolved precipitates during cyclic welding thermal history.[38,39] Figure 3(d) shows a mixed microstructure in the ICHAZ-AW, which is mainly composed of equiaxed ferrites, pearlites, and carbides. It could be seen from Figure 3(h) that the microstructure in ICHAZ-SW is basically the same as that of ICHAZ-AW. Combined with the profiles of micro Vickers hardness, it is indicated that the well-designed simulated welding could better reflect and replicate the characteristics of the actual welding HAZ.

Following PWHT, the average micro Vickers hardness distribution characteristics across the HAZ in both A6 and S6 are plotted in Figure 4 for comparison. Quantitative results of HAZ micro Vickers hardness values in both A6 and S6 are basically consistent, showing a gradual decrease from the CGHAZ to the ICHAZ, which is largely similar to the changing trend of the as-welded state. Concurrently, the micro Vickers hardness difference between each sub-zone of the HAZ is also significantly reduced after PWHT. It is implied that a homogenized HAZ with uniform micro Vickers hardness values can be obtained *via* tempering at high temperature.[34] However, as shown by the black rectangles in Figure 4, a dip in the micro Vickers hardness profile (169.9 ± 4.6 HV0.2 in A6 and 171.9 ± 6.8 HV0.2 in S6), which is identified as the soft zone, is found in the FGHAZ close to the ICHAZ. It is observed clearly that the width of the soft zone in SW (0.75 mm) is almost twice as larger as that in AW (0.45 mm), which could be helpful to identify and investigate the characteristics of the soft zone during subsequent creep test.

Furthermore, as shown in Figure 5, distributions of main alloying elements including C, Cr, and Mo in the soft zone of A6 and S6 have been measured by means of EPMA-WDS, which illustrates the partitioning behavior of the alloying elements into the matrix and carbides. Figures 5(a) and (b) display typical SE and BSE images in the soft zone of A6, whose microstructure is composed of blocky ferrites and coarse carbides. Similarly, as shown in Figures 5(f) and (g), the microstructure in the soft zone of S6 also consists of blocky ferrites and carbides. Segregation of alloying elements leads to white and gray contrast due to different etching behaviors. The white area is the carbide aggregation region, and the content of alloy elements is higher than that of the gray region.[40] The concentration distribution in the enrichment and dilution regions of A6 and S6 is exhibited in Figures 5(c) through (e) and (h) through (j), respectively. It can be seen that coarsened carbides in A6 and S6 show highly concentrated C, Cr, and Mo contents, whereas their respective contents in the matrix are low. These results imply that both typical microstructures and major alloying element distribution of A6 and S6 are highly consistent.

In the present investigation, a novel and effective method has been proposed and verified to identify the precise location of the soft zone of 1.25Cr-Mo heat-resistant steel by Gleeble simulation. The enlarged soft zone could potentially enable enriched understanding of creep fracture mechanisms during long-term creep tests. The conclusions are summarized as follows:

1. The micro Vickers hardness distributions of the HAZ in both AW and SW show the same trend, gradually decreasing from 320 HV0.2 of the CGHAZ to 200 HV0.2 of the IGHAZ. Concurrently, both the total width of the HAZ in the SW and divided width of each sub-zone are approximately 3 times wider than those of AW.
2. Comparing AW with SW, the heterogeneous microstructural features of corresponding sub-zones of the HAZ are consistent. The microstructure of the CGHAZ mainly comprises bainitic laths and bainitic granules within coarse PAGs (110 μm). Similarly, the FGHAZ is made up of bainites and carbides within fine equiaxed PAGs (30 μm). The ICHAZ grains are primarily composed of a mixture of equiaxed ferrites, pearlites, and carbides.
3. After PWHT, the soft zone, which shows a dip (169.9 ± 4.6 HV0.2 in A6 and 171.9 ± 6.8 HV0.2 in S6) in the micro Vickers hardness profile, could be accurately positioned in the region of the FGHAZ adjacent to the ICHAZ. Combined with the results of EPMA, it is indicated that both A6 and S6 show similar microstructures and alloying element distributions in the soft zone.

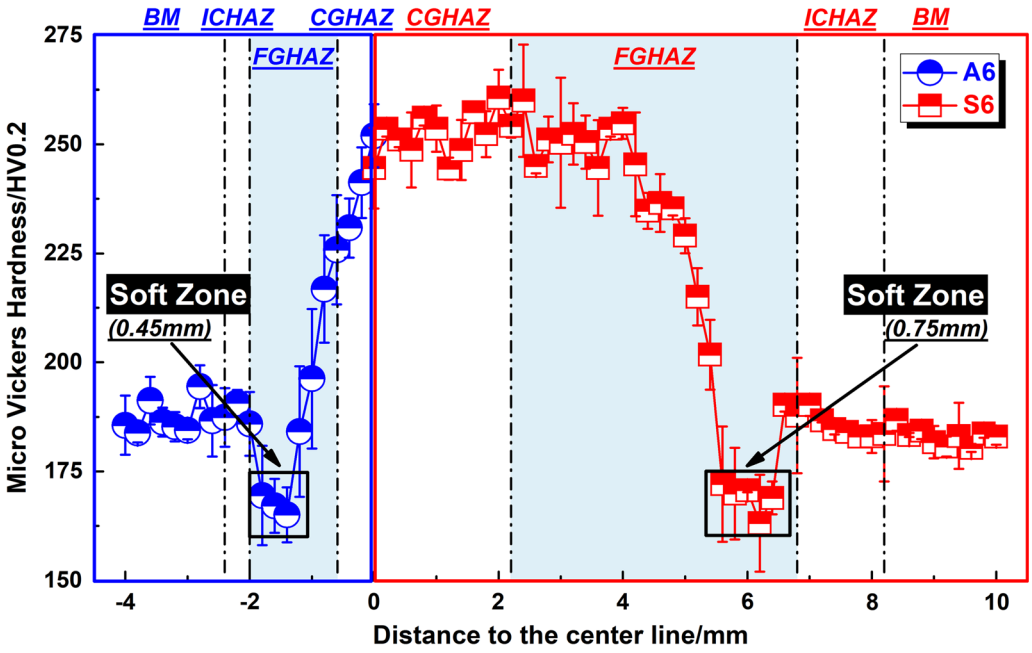

Fig. 4—Micro Vickers hardness profiles across the entire HAZ in A6 and S6 weldments. (Black rectangles represent soft zone).

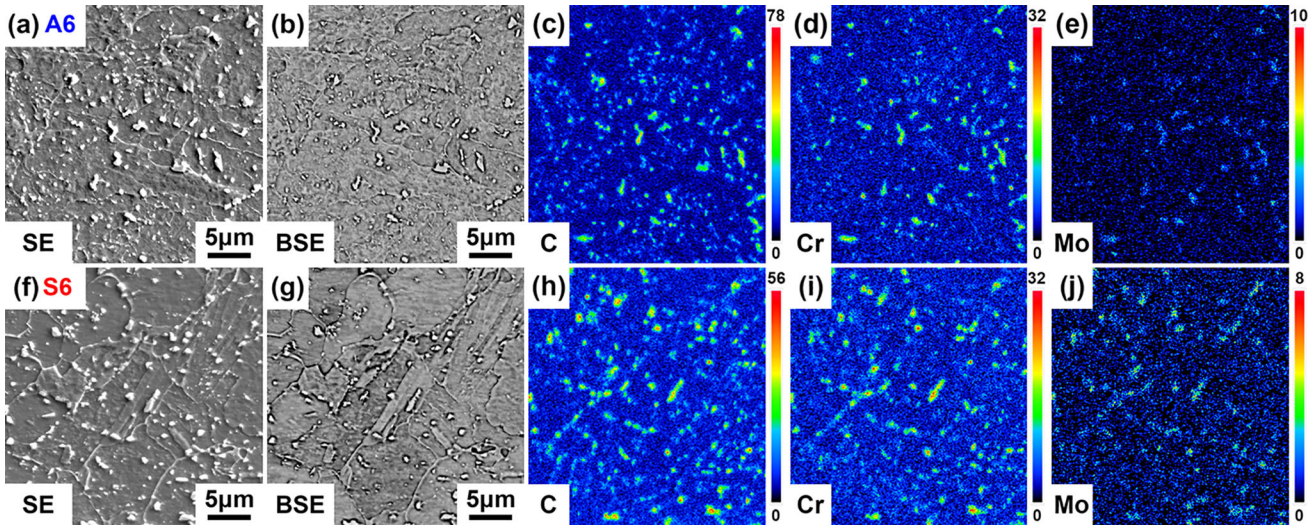

Fig. 5—EPMA results of C, Cr, and Mo for precipitates of the soft zone in (*a*) through (*e*) A6 and (*f*) through (*j*) S6.

ACKNOWLEDGMENTS

The authors wish to thank the financial supports from National Natural Science Foundation of China (Grant Nos. U20A20277, 52050410341, 51861130361, 51861145312, and 52011530180), Newton Advanced Fellowship by the Royal Society (Grant No. RP12G0414), Royal Academy of Engineering (Grant No. TSPC1070), The Fundamental Research Fund for Central Universities (Grant No. N2025025), Natural Science Foundation of Liaoning (Grant No. 2019KF0502), Regional Innovation Joint Fund of Liaoning Province (Grant No. 2020-YKLH-39), Special Fund for Key Program of Science and Technology of Liaoning Province (Grant No. 2019JH1/10100014), and Xingliao Talents Program (Grant Nos. XLYC1807024 and XLYC1802024).

REFERENCES

1. M.Y. Kim, M.G. Jo, J.Y. Suh, W.S. Jung, and J.H. Shim: *Mater. Charact.*, 2020, vol. 163, art. no. 110314. https://doi.org/10.1016/j.matchar.2020.110314.
2. B. Raj, B.K. Choudhary, and R.K. Singh Raman: *Int. J. Press. Vessels Pip.*, 2004, vol. 81, pp. 521–34.
3. I. Souza Bott, L.F.G. Souza, J.C.F. Jorge, J.C.G. Teixeira, and R.P. Rocha Paranhos: *Mater. Charact.*, 2005, vol. 54, pp. 206–15.
4. D.J. Abson and J.S. Rothwell: *Int. Mater. Rev.*, 2013, vol. 58, pp. 437–73.
5. J.A. Francis, G.M.D. Cantin, W. Mazur, and H.K.D.H. Bhadeshia: *Sci. Technol. Weld. Joi.*, 2009, vol. 14, pp. 436–42.

6. C. Pandey, M.M. Mahapatra, P. Kumar, and N. Saini: *Metall. Mater. Trans. B*, 2018, vol. 49B, pp. 2881–95.
7. K. Laha, K. Chandravathi, P. Parameswaran, and K.B.S. Rao: *Metall. Mater. Trans. A*, 2009, vol. 40A, pp. 386–97.
8. J.A. Francis, W. Mazur, and H.K.D.H. Bhadeshia: *Mater. Sci. Technol.*, 2006, vol. 22, pp. 1387–95.
9. Y. Wang, R. Kannan, and L. Li: *Mater. Charact.*, 2016, vol. 118, pp. 225–34.
10. Z. Wang, J. Wu, J. Li, X. Wu, Y. Huang, and X. Li: *Metall. Mater. Trans. A*, 2018, vol. 49A, pp. 187–97.
11. X. Xu, G.D. West, J.A. Siefert, J.D. Parker, and R.C. Thomson: *Metall. Mater. Trans. A*, 2018, vol. 49A, pp. 1211–30.
12. Y. Wang, W. Zhang, H. Huang, Y. Wang, W. Zhong, J. Chen, and Z. Feng: *Scripta Mater.*, 2021, vol. 194, art. no. 113640. https://doi.org/10.1016/j.scriptamat.2020.113640.
13. Y. Wang, W. Zhang, Y. Wang, Y.C. Lim, X. Yu, and Z. Feng: *Mater. Sci. Eng. A*, 2021, vol. 799, art. no. 140356. https://doi.org/10.1016/j.msea.2020.140356.
14. J. Parker: *Mater. Sci. Eng. A*, 2013, vol. 578, pp. 430–37.
15. Y. Liu, S. Tsukamoto, K. Sawada, and F. Abe: *Metall. Mater. Trans. A*, 2014, vol. 45A, pp. 1306–14.
16. S. Fujibayashi: *ISIJ Int.*, 2007, vol. 47, pp. 333–39.
17. K. Shinozaki, D.-J. Li, H. Kuroki, H. Harada, and K. Ohishi: *ISIJ Int.*, 2002, vol. 42, pp. 1578–84.
18. N.D. Raath, D. Norman, I. Mcgregor, S. Hepple, R. Dashwood, and D.J. Hughes: *Metall. Mater. Trans. A*, 2018, vol. 49A, pp. 1536–51.
19. K. Sawada, M. Bauer, F. Kauffmann, P. Mayr, and A. Klenk: *Mater. Sci. Eng. A*, 2010, vol. 527, pp. 1417–26.
20. S.A. David, J.A. Siefert, and Z. Feng: *Sci. Technol. Weld. Joi.*, 2013, vol. 18, pp. 631–51.
21. M.E. Abd El-Azim, O.H. Ibrahim, and O.E. El-Desoky: *Mater. Sci. Eng. A*, 2013, vol. 560, pp. 678–84.
22. K. Laha, K.S. Chandravathi, P. Parameswaran, K.B.S. Rao, and S.L. Mannan: *Metall. Mater. Trans. A*, 2007, vol. 38A, pp. 58–68.
23. C. Pandey, M.M. Mahapatra, P. Kumar, S. Kumar, and S. Sirohi: *J. Mater. Process. Technol.*, 2019, vol. 266, pp. 140–54.
24. S. Fujibayashi and T. Endo: *ISIJ Int.*, 2003, vol. 43, pp. 790–97.
25. S. Albert, M. Matsui, H. Hongo, T. Watanabe, K. Kubo, and M. Tabuchi: *Int. J. Press. Vessels Pip.*, 2004, vol. 81, pp. 221–34.
26. A. Bhaduri, C. Das, S. Albert, A. Klenk, and B. Murty: *Mater. Manuf. Process.*, 2011, vol. 26, pp. 62–65.
27. Y. Shen and C. Wang: *Metall. Mater. Trans. B*, 2019, vol. 50B, pp. 595–600.
28. Y. Shen, H. Matsuura, and C. Wang: *Metall. Mater. Trans. A*, 2018, vol. 49A, pp. 4413–18.
29. J.B. Kim, T.H. Lee, and I. Sohn: *Metall. Mater. Trans. A*, 2018, vol. 49A, pp. 2705–20.
30. C.A. Schneider, W.S. Rasband, and K.W. Eliceiri: *Nat. Methods*, 2012, vol. 9, pp. 671–75.
31. Y. Shen, J. Leng, and C. Wang: *J. Mater. Sci. Technol.*, 2019, vol. 35, pp. 1747–52.
32. Y. Wang and L. Li: *Weld. J.*, 2016, vol. 95, pp. 27–36.
33. X. Xu, A. Benaarbia, D.J. Allen, M.A.E. Jepson, and W. Sun: *Mater. Sci. Eng. A*, 2020, vol. 791, art. no. 139546. https://doi.org/10.1016/j.msea.2020.139546.
34. Y. Wang, L. Li, and R. Kannan: *Mater. Sci. Eng. A*, 2018, vol. 714, pp. 1–13.
35. M. Lomozik and I. Kubiszyn: *Weld. Int.*, 2006, vol. 20, pp. 257–61.
36. Y. Shen, B. Chen, and C. Wang: *Metall. Mater. Trans. A*, 2021, vol. 52A, pp. 14–19.
37. Y. Shen, B. Chen, and C. Wang: *Metall. Mater. Trans. A*, 2020, vol. 51A, pp. 3371–76.
38. X. Yu, S.S. Babu, H. Terasaki, and Y. Komizo: *Acta Mater.*, 2013, vol. 61, pp. 2194–2206.
39. F. Abe, T.-U. Kern, and R. Viswanathan: *Creep-Resistant Steels*, 1st ed., Elsevier, Amsterdam, 2008, pp. 19–42.
40. J. Laigo, F. Christien, R. Le Gall, F. Tancret, and J. Furtado: *Mater. Charact.*, 2008, vol. 59, pp. 1580–86.